




The Use of Radiomics Data Obtained from ADC Map of Lumbar MRI and Machine Learning in Diagnosis of Osteoporosis

Fatih Erdem ^{1,*}, Emrah Akay², Gulen Demirpolat², Bahar Yanık Keyik², Erdogan Bulbul²

¹ Department of Pediatric Radiology, Ankara University Hospital, Ankara, Turkey

² Balıkesir University Hospital, Balıkesir, Turkey

*Corresponding Author: Department of Pediatric Radiology, Ankara University Hospital, Ankara, Turkey. Email: mdfatiherdem@gmail.com

Received: 13 April, 2024; Revised: 29 June, 2024; Accepted: 16 July, 2024

Abstract

Background: Osteoporosis is a systemic skeletal disorder marked by reduced bone density and microarchitectural deterioration, leading to increased fracture risk. While the DEXA scan is the WHO-recommended diagnostic standard, its limitations necessitate alternative methods. Emerging magnetic resonance imaging (MRI) techniques, radiomics, and machine learning promise to enhance osteoporosis diagnosis through detailed analysis of lumbar MRI apparent diffusion coefficient (ADC) maps, potentially revolutionizing early detection and treatment strategies.

Objectives: In this study, we are going to evaluate the performance of machine learning (ML) models using radiomics features of lumbar MRI ADC map for osteoporosis detection, and to identify significant features and their diagnostic thresholds. Specific performance metrics such as accuracy, sensitivity, specificity, and Area Under the receiver operating characteristic (ROC) Curve (AUC) were assessed.

Patients and Methods: Patients and Methods: This retrospective study employed a cross-sectional design, with a total of 140 cases, including 21 with osteoporosis. The study's inclusion criteria consisted of concurrent lumbar MRI and DEXA within a year, while exclusion criteria included infectious or neoplastic lumbar lesions, fractures, instrumentation, significant osteodegenerative changes, cases where the first four lumbar vertebrae were not included in the imaging field, and absence of diffusion-weighted imaging. Manual segmentation of lumbar vertebrae from ADC maps was performed to create a comprehensive dataset, comprising 5,580 radiomics features per case. Subsequently, the top five features selected by fast correlation-based filter (FCBF) were used to test the performance of seven Machine Learning algorithms (k-Nearest neighbors, decision tree, random forest, logistic regression, support vector machine, naive bayes, and neural network). Statistical tests and ROC curve analysis were conducted to determine the significance and thresholds of these features.

Results: The study included 140 cases, with 132 females (94.3%) and 8 males (5.7%), and a mean age of 65.32 ± 8.50 years. The mean BMI was 31.43 ± 5.53 kg/m² for females and 26 ± 3.59 kg/m² for males. In terms of demographic differences, no significant age difference was found between the osteoporotic and non-osteoporotic groups ($P = 0.889$). However, the osteoporotic group had significantly lower mean body weight (64.90 ± 10.13 kg vs. 74.68 ± 13.94 kg, $P = 0.003$) and BMI (27.40 ± 4.38 kg/m² vs. 31.77 ± 5.52 kg/m², $P = 0.001$) compared to the non-osteoporotic group. The median interval between DEXA and lumbar MRI was 1 month (range 0.1 - 11.87 months). The Neural Network model demonstrated the highest performance with an AUC of 0.616 and a classification accuracy of 0.764 using all features. The Naive Bayes model, using the top five features selected by FCBF, showed the highest performance with an AUC of 0.913, accuracy of 0.907, sensitivity of 0.667, and specificity of 0.95. All ML models' performance were elevated by feature selection. Independent *t*-tests and Mann-Whitney U tests identified 521 and 670 significant features, respectively ($P < 0.05$). ROC analysis revealed 58 features with AUC values above 0.70.

Conclusion: This study's findings suggest that ML models, particularly the Naive Bayes algorithm, can effectively use lumbar ADC map radiomics to diagnose osteoporosis. These findings could enhance early detection and treatment strategies, potentially improving patient outcomes and reducing the burden of osteoporotic fractures. This study also established threshold values for significant features.

Keywords: Radiomics, Machine Learning, Lumbar MRI, Diffusion Weighted Imaging, Osteoporosis

1. Background

Osteoporosis is a systemic skeletal disease characterized by decreased bone density and impairment in bone tissue microarchitecture, causing more fragile bones and a greater likelihood of fractures (1). Osteoporosis is a common public health problem worldwide, and it depends on many factors, such as ethnicity, gender, age, nutritional status, drug use, and diseases affecting bone density (1, 2). Osteoporosis and osteoporotic fractures have undesirable consequences on the individual and society in terms of financial, psychosocial, physical, and quality of life aspects (1, 2). This is why early diagnosis of osteoporosis, especially before the development of fractures, is essential.

World Health Organization (WHO) adopted the bone mineral density (BMD) test with dual-energy X-ray absorptiometry (DEXA) as a reference standard in 1994 (3). The T-score, which reflects how much standard deviation (SD) above or below the mean BMD of a young, healthy white woman, is used by WHO to identify osteoporosis. When the T-score is -2.5 SD or less, osteoporosis is diagnosed (2). While DEXA is economical and non-invasive, it has low sensitivity to predict fractures and involves low-dose ionizing radiation (4, 5). Furthermore, it has some limitations, such as the possibility that reference data for BMD provided by manufacturers may not be appropriate for local populations, being affected by body size, osteodegenerative changes, vascular calcifications, prior injected contrast media, fractures and deformities, two-dimensional measurement of BMD, and operator dependency (4, 6). Other imaging modalities such as quantitative computed tomography (QCT), quantitative ultrasound (QUS), and high-resolution peripheral quantitative computed tomography (HR-pQCT) emerged as a probable alternative to DEXA. Quantitative computed tomography provides 3D imaging and accurate bone density measurements but is limited by higher radiation doses and costs. Quantitative computed tomography is portable and radiation-free, suitable for screening but less accurate than DEXA and QCT. High-Resolution peripheral quantitative computed tomography offers detailed bone microarchitecture assessment, improving fracture prediction and monitoring therapy, but its use is restricted by high costs and limited availability (7-9).

Many studies in the literature have evaluated and demonstrated the use of various magnetic resonance imaging (MRI) techniques in the diagnosis of osteoporosis. In osteoporotic bone, the proportion of adipose tissue increases as bone production declines, which is thought to be caused by the differentiation of stromal cells into adipocytes rather than osteoblasts (10, 11). The amount of fat, protein, water, and bone cells determines how the bone marrow appears on the MRI sequence (5, 12-20). Among these studies, the apparent diffusion coefficient (ADC) values decreased in osteoporotic patients, which was hypothesized to be related to a decrease in diffusion due to the narrowing of the extracellular space as a result of increasing adipose tissue (5, 12, 15, 16, 19, 20). Apparent diffusion coefficient denotes a biological tissue's particular diffusion capacity, microscopic structure, and organization (21).

Radiomics and machine learning (ML) offer novel approaches for osteoporosis diagnosis by extracting high-dimensional data from medical images, which traditional methods might overlook. Radiomics can quantify tissue heterogeneity and capture subtle changes in bone microarchitecture, while ML algorithms can analyze these complex data sets to identify patterns indicative of osteoporosis (14, 17, 22, 23). These techniques could complement existing diagnostic methods, such as DEXA, by providing more detailed and accurate assessments of bone health (22). Early and accurate detection of osteoporosis using these advanced techniques could potentially lead to better clinical outcomes by enabling timely intervention and personalized treatment plans, thus reducing the risk of fractures and associated complications.

2. Objectives

The primary objective of this study is to evaluate the diagnostic performance of various ML models, specifically naive bayes and neural networks, in identifying osteoporosis using radiomics features extracted from lumbar MRI ADC maps. This will be measured using performance metrics such as AUC, accuracy, sensitivity, specificity, F1 score, and recall. Additionally, the secondary objective is to identify the most significant radiomics features that contribute to accurate osteoporosis diagnosis. The hypotheses

guiding this study are: (1) machine learning models can significantly improve the diagnostic accuracy of osteoporosis compared to traditional methods; and (2) specific radiomics features from lumbar MRI ADC maps are significantly associated with osteoporosis and can reliably differentiate between osteoporotic and non-osteoporotic cases. These objectives and hypotheses are designed to provide a comprehensive evaluation of the potential of ML in enhancing osteoporosis diagnosis, with a focus on both model performance and feature significance.

3. Patients and Methods

3.1. Study Design and Patient Selection

This cross-sectional study retrospectively scanned cases referred to the Radiology Department between 01/01/2015 and 31/12/2020. Lumbar MRIs were obtained from a Philips Ingenia 1.5T MRI system (Philips, Best, Netherlands), and BMD measurements were acquired using a DEXA device (Lunar Prodigy, model 8743; GE Lunar, Madison, WI, USA). Lumbar MRIs and DEXA examinations from the same patients, performed within one year of each other, were included unless they met the exclusion criteria.

Exclusion criteria were as follows:

- (1) Interval exceeding one year between lumbar MRI and DEXA examinations,
- (2) Presence of an infectious or neoplastic lesion in any lumbar vertebral body,
- (3) Fracture of a lumbar vertebral body, instrumentation, or osteodegenerative changes that could impair the measurements,
- (4) Cases in which the first four lumbar vertebrae were not included in the imaging field,
- (5) Absence of diffusion-weighted imaging.

The study continued with 140 participants, 21 of whom had osteoporosis, after exclusion (Figure 1). The cases' height and weight were recorded. Anterior-posterior lumbar vertebrae BMD was routinely measured. The DEXA scan used L1-4 as the basis for T-scores. The cases were classified as "osteoporosis" if the T-score was ≤ -2.5 , and "non-osteoporosis" if the T-score was > -2.5 .

3.2. Image Acquisition

The lumbar MRI diffusion-weighted imaging sequence was acquired axially on a Philips Ingenia 1.5T MRI device (Philips, Best, Netherlands). The sequence utilized a spin-echo technique with fat suppression (SPIR) and a parallel imaging method (SENSE). The pulse repetition time was 7505 milliseconds, the echo time was 60 milliseconds, and the echo train length was 43. The slice thickness was 3 mm, with a 3 mm gap between slices. The field of view (FOV) was $225 \times 225 \text{ mm}^2$, and the b-values were 0 and 650 s/mm^2 .

The PACS software available in our hospital was used as the archiving system. Lumbar MRI diffusion-weighted images (b-values of 0 and 650 s/mm^2) of the cases that met the criteria were transferred to the 3DSlicer 4.8.1 program in DICOM (Digital Imaging and Communications in Medicine) format. First, monoexponential ADC maps were created with the module named DWModeling.

3.3. Segmentation

Segmentation was performed manually by an experienced board-certified radiologist. To ensure consistency, the intraobserver reliability was evaluated using the intraclass correlation coefficient (ICC), which measured the absolute agreement between the features obtained from two separate segmentation sets performed at a one-month interval. Features that achieved good ($0.75 \leq \text{ICC} < 0.9$) to excellent ($\text{ICC} \geq 0.9$) intraobserver reliability were considered stable.

The contours were meticulously drawn to closely follow the cortical bone while remaining within the boundaries of the vertebral body. Each vertebral level was segmented separately and named as L1, L2, L3, and L4. Additionally, inspired by the DEXA assessment, which provides average bone mineral density values for L1, L2, L3, and L4 levels, the segmentations were combined into two separate sets: L1-4 and L2-4. Consequently, a total of six segmentations—L1, L2, L3, L4, L1-4, and L2-4—were obtained for each case (Figure 2).

3.4. Preprocessing and Radiomics Feature Extraction

Following the segmentation process, features were extracted from segmented volumes using the PyRadiomics-based Radiomics module. Prior to feature extraction, a consistent configuration was applied across all cases. Specifically, under the module's "resampling and filtering" section, the bin width was

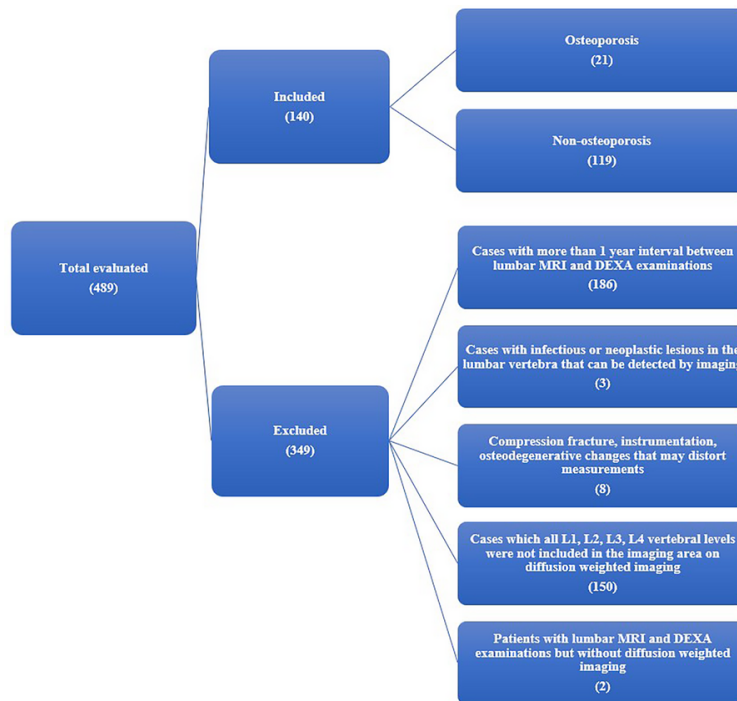


Figure 1. Patients' enrollment diagram

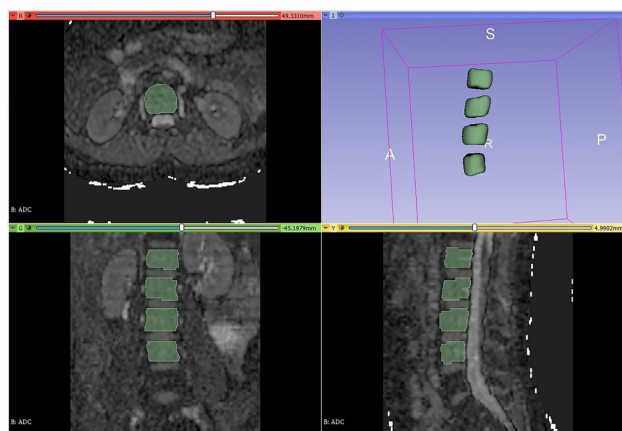


Figure 2. Segmentation process on 3D Slicer software of lumbar vertebrae

fixed at 25. Additionally, the Laplacian of gaussian filter kernel size was set to 3 mm, and wavelet-based features were enabled to generate transformed filtered images. This standardization aimed to achieve uniformity

among cases, increase the volume of data, and capture high dimensionality in the radiomics dataset.

Subsequently, for each of the L1, L2, L3, L4, L1-4, and L2-

4 segmentations, the following features were extracted:

- First-order features (18 features) from the original images
- Second-order features based on gray level co-occurrence matrix (GLCM) (24 features)
- Second-order features based on gray level dependence matrix (GLDM) (14 features)
- High-order features based on gray level run length matrix (GLRLM) (16 features)
- High-order features based on gray level size zone matrix (GLSZM) (16 features)
- High-order features based on neighborhood gray-tone difference matrix (NGTDM) (10 features)

Additionally, features were extracted from Laplacian of Gaussian-filtered images with a kernel size of 3 mm:

- First-order features (18 features)
- Second-order features based on GLCM (24 features)
- Second-order features based on GLDM (9 features)
- High-order features based on GLRLM (16 features)
- High-order features based on GLSZM (16 features)
- High-order features based on NGTDM (5 features)

Furthermore, a total of 744 features were obtained from wavelet-transformed images for each case, resulting in a grand total of 5,580 features across all cases.

3.5. Feature Selection, Model Validation, Classification, and Performance Evaluation

For classification using ML algorithms, the [Orange](#) data mining program version 3.30 was employed. The dataset consisted of 5,580 features and 140 cases, which were subjected to classification using seven distinct ML algorithms: k-nearest neighbors (kNN), decision tree, random forest, logistic regression, support vector machine (SVM), naive bayes, and neural network. The classification was performed both before and after the feature selection process using these seven ML algorithms to evaluate the positive effect of feature selection on the performance metrics.

In this study, we used the fast correlation-based filter (FCBF) method to select five features from the extracted radiomics data. The choice of five features was based on preliminary experiments, aiming to balance the trade-off between reducing dimensionality and retaining significant predictive power. This approach helps mitigate the risk of overfitting by focusing on the most

relevant features while avoiding the inclusion of redundant or less informative ones. We recognize that the optimal number of features may vary with different datasets and encourage further research to explore this aspect.

The ML models were validated using 10-fold cross-validation to ensure robust evaluation. This method involves dividing the dataset into ten equal parts, with each part used as a validation set while the remaining nine parts are used for training. This process is repeated ten times, with each part serving as the validation set once. The performance metrics were calculated by averaging the results from each fold, providing a more reliable estimate of the model's performance compared to a single train-test split.

The performance metrics, including AUC (Area Under the Curve), classification accuracy (CA), F1 score, precision (positive predictive value), recall (sensitivity), and specificity, were calculated for each fold. These metrics provide a comprehensive evaluation of the model's diagnostic capabilities, measuring its ability to correctly identify positive and negative cases of osteoporosis. The use of cross-validation ensures that the models are not overfitted to a particular subset of the data and can generalize well to unseen data.

3.6. Conventional Statistical Analysis

IBM SPSS Statistics for Windows, version 22 (IBM Corp., Armonk, NY, USA), was used for conventional statistical analysis. After evaluating the ML model performance, independent samples *t*-test and Mann-Whitney U test were performed to determine whether each feature showed a statistically significant difference in osteoporosis status. The normal distribution of data was assessed using the Kolmogorov-Smirnov test and histogram graphs. Means and SDs for normally distributed data and medians and interquartile ranges for non-normally distributed data were expressed as mean \pm SD and median (interquartile range), respectively. Categorical data were expressed as counts and percentages.

Receiver Operating Characteristic curve analysis was performed for features found to be significant in these tests, and threshold values were determined. Threshold values for significant radiomics features were established using the Youden index. The Youden index was employed to identify the optimal cut-off points that

maximize the sum of sensitivity and specificity, thereby ensuring balanced and effective discrimination between osteoporotic and non-osteoporotic cases. A P-value of < 0.05 was considered significant in all statistical results.

3.7. Ethical Considerations

This study was approved by the Clinical Research Ethics Committee of Balikesir University Faculty of Medicine on 26/05/2021, with the decision number 2021/129. Informed consent was not required due to the retrospective nature of the study.

4. Results

A total of 140 cases (132 females, 8 males; mean age 65.32 ± 8.50 years) were included. For women, the mean age was 65.20 ± 8.19 years, and for men, it was 67.22 ± 13.28 years. Female subjects had a median height of 1.53 ± 0.08 m, mean body weight of 73.21 ± 13.81 kg, and mean BMI of 31.43 ± 5.53 kg/m². Male subjects had a mean height of 1.67 ± 0.08 m, mean body weight of 73.25 ± 15.64 kg, and mean BMI of 26 ± 3.59 kg/m².

Age, body weight, and BMI fit a normal distribution for all cases and by gender, except height, which was normally distributed only for males. An independent samples *t*-test showed no significant age difference between osteoporotic and non-osteoporotic groups ($P = 0.889$), but body weight and BMI were significantly different ($P = 0.003$ and $P = 0.001$, respectively). The osteoporotic group had lower mean body weight (64.90 ± 10.13 kg) and BMI (27.40 ± 4.38 kg/m²) compared to the non-osteoporotic group (74.68 ± 13.94 kg and 31.77 ± 5.52 kg/m²) (Table 1). No significant difference in height was found ($P = 0.412$).

The median interval between DEXA and lumbar MRI was 1 month (max 11.87 months) (Figure 3).

The neural network was the top-performing ML model using 5,580 radiomics features for osteoporosis detection (AUC 0.616, CA 0.764, F1 score 0.108, precision 0.125, recall 0.095, specificity 0.882) (Figure 4). Feature selection with FCBF improved performance across seven ML models (Table 2), with Naive Bayes achieving the highest performance (AUC 0.913, CA 0.907, F1 score 0.683, precision 0.7, recall 0.667, specificity 0.95) (Tables 3, 4 and Figure 5A and B).

All features had ICC values > 0.75, indicating reliability. Independent samples *t*-test and Mann-Whitney U tests identified 521 and 670 significant

features ($P < 0.05$) for osteoporosis status, respectively. Receiver operating characteristic (ROC) analysis showed 58 features with AUC > 0.70, predominantly from wavelet-transformed images (42 features), mainly from the LHL subvolume (30 features) and the L1 vertebra level (38 features). The Youden index determined threshold values for these features, with corresponding sensitivity and specificity provided (Table 5).

Among these 58 features, 30 belonged to the L1 vertebra level and were obtained from images created by wavelet transformation. Of these 30 features, 9 were first-order, 8 were GLCM-based, 3 were GLDM-based, 5 were GLRLM-based, 4 were GLSZM-based, and 1 was NGTDM-based.

5. Discussion

Our study is the only study to predict osteoporosis using radiomics features obtained from lumbar MRI ADC maps and ML algorithms. Additionally, it is the only study that examines whether each of these radiomics features shows a statistically significant difference in osteoporosis, aiming to find a threshold value for those that show significant differences.

The neural network model demonstrated low performance metrics, including an AUC of 0.616, an F1 score of 0.108, and a recall of 0.095, despite being identified as the best model when utilizing all features. Several factors may explain this outcome. Firstly, the significant class imbalance in the dataset likely biased the model toward the majority class, impairing its ability to accurately predict the minority class. Secondly, the small dataset size limited the model's capacity to generalize and effectively learn from the data. Neural networks typically require large volumes of data to achieve optimal performance, and the lack of sufficient data may have hindered the model's efficacy. Additionally, the complexity of neural networks means they are highly sensitive to hyperparameter settings, and inadequate tuning could result in suboptimal model configurations.

Moreover, the model might have been prone to overfitting due to the high dimensionality of the feature set and the relatively small sample size. Overfitting occurs when the model learns noise and details from the training data to an extent that negatively impacts its performance on new, unseen data. This can be particularly problematic in complex models like neural

Table 1. Comparison of Age, Body Weight and Body Mass Index Between Osteoporotic and Non-osteoporotic Subjects

Variables	Independent samples t-test (t-test for equality of means)		
	Sig. (2-tailed)	Mean difference	Std. error difference
Age	0.889	-0.28	2.02
Body weight (kg)	0.003	-9.78	3.18
BMI (kg/m ²)	0.001	-4.37	1.27

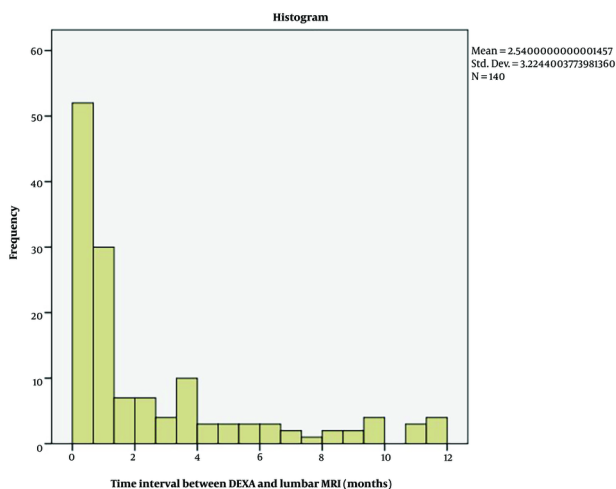


Figure 3. Histogram plot showing frequencies of time interval between dual-energy X-ray absorptiometry (DEXA) and lumbar MRI

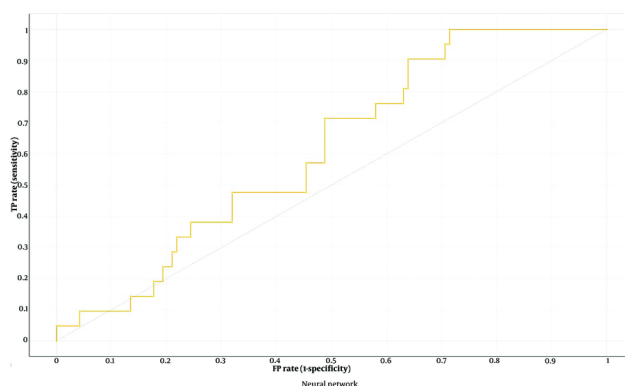


Figure 4. Receiver operating characteristic (ROC) curve of the neural network model formed with all radiomics features (5580 radiomics features)

networks, which have a high capacity to fit the training data too closely. These findings highlight the importance of addressing class imbalance, ensuring

sufficient data volume, performing rigorous hyperparameter optimization, and implementing techniques to prevent overfitting in future studies to

Table 2. The Selected Five Features and their Definitions

Radiomics feature ^a	Definition
L1-4 log-sigma-3-0-mm-3D GLCM sum squares	The sum of squares or Variance is a measure of the mean intensity level in the GLCM in the distribution of neighboring intensity level pairs. The L1-4 label represents the related segmented vertebral level. It was obtained from the images created by choosing the Laplacian of Gaussian filter 3 mm.
L3 log-sigma-3-0-mm-3D first order minimum	First order minimum is the minimum grey level value in the image. The L3 label represents the related segmented vertebral level. It was obtained from the images created by choosing the Laplacian of Gaussian filter 3 mm.
L3 wavelet-LLH first order Mean	First order mean is the average grey level value in the image. The L3 label represents the related segmented vertebral level. It was obtained from the images created by wavelet transform. LLH is one of the 8 sub volumes in the 3D wavelet transform.
L1 wavelet-LHH GLSZM large area high gray level emphasis	LAHGLE measures the ratio in the image of the co-distribution of larger sized regions with higher grey level values. The L1 label represents the related segmented vertebral level. It was obtained from images created by wavelet transform. LHH is one of the 8 sub volumes in the 3D wavelet transform.
L2 log-sigma-3-0-mm-3D GLCM IDN	One of the measures of an image's local homogeneity is IDN (inverse difference normalized). Unlike homogeneity, IDN normalizes the difference in intensity values between neighbors by dividing it by the total number of discrete intensity values. The L2 label represents the related segmented vertebral level. It was obtained from the images created by choosing the Laplacian of Gaussian filter 3 mm.

Abbreviations: GLSZM, gray level size zone matrix; GLCM, gray level co-occurrence matrix.

^a The 5 features selected by fast correlation-based filter (FCBF).

Table 3. The Performance Values of Machine Learning Models Formed with the Five Selected Features by Fast Correlation-Based Filter ^a

Variables	AUC	CA	F1	Precision	Recall	Specificity
ML Algorithm						
Naive Bayes	0.913	0.907	0.683	0.7	0.667	0.95
Neural Network	0.752	0.864	0.296	0.667	0.19	0.983
Random Forest	0.743	0.864	0.345	0.625	0.238	0.975
SVM	0.738	0.857	0.091	1	0.048	1
Logistic Regression	0.722	0.864	0.296	0.67	0.19	0.983
kNN	0.709	0.85	0.16	0.5	0.095	0.983
Decision Tree	0.654	0.8	0.333	0.333	0.333	0.882

Abbreviation: ML, machine learning; AUC, area under the curve; SVM, support vector machine; KNN, k-nearest neighbors.

^a The performance of ML algorithms.

Table 4. Confusion Matrix for the Naive Bayes Model (5 Features) ^a

Variable	Predicted		Total
	Osteoporotic	Non-osteoporotic	
Actual			
Osteoporotic	14 (10)	7 (5)	21
Non-osteoporotic	6 (4)	113 (81)	119
Total	20	120	140

^a Confusion matrix for the Naive Bayes model (showing number of instances and percentages).

enhance the predictive performance of neural networks in similar applications.

The Naive Bayes model showed significant improvement after feature selection, achieving an AUC of 0.913. This improvement can be attributed to several factors. Feature selection likely removed irrelevant or redundant features, reducing the dimensionality of the

data and allowing the model to focus on the most informative variables. This process enhances the model's ability to generalize from the training data to new, unseen data by minimizing the risk of overfitting.

In the clinical context, this improvement is particularly relevant. A higher AUC indicates a better ability of the model to distinguish between osteoporotic

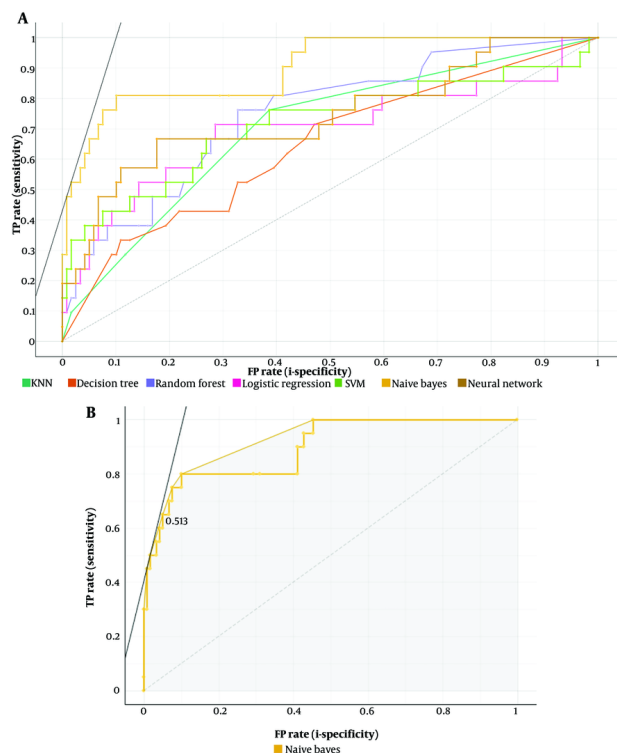


Figure 5. Receiver operating characteristic (ROC) curves of the all seven ML model, (A); and the Naive Bayes model only, (B). (Abbreviations: kNN, k-nearest neighbors; SVM, support vector machine).

and non-osteoporotic cases, which is crucial for early diagnosis and intervention. By identifying the most significant features, clinicians can better understand the underlying factors contributing to osteoporosis, leading to more targeted and effective treatment strategies. Additionally, the use of a more accurate model in clinical practice can improve patient outcomes by enabling more precise and reliable diagnostic processes. Thus, the feature selection process not only enhances the performance of the Naive Bayes model but also has meaningful implications for improving the clinical management of osteoporosis. Future studies should continue to explore and validate these selected features to ensure their robustness and relevance in diverse patient populations.

To our knowledge, there are few studies on osteoporosis prediction using ML and radiomics data obtained from DEXA, MRI, and CT. In the study by Rastegar et al., which included 147 cases and aimed to differentiate osteoporotic, osteopenic, and normal BMD

using ML models based on radiomics data from DEXA, the most successful combinations showed AUC values of 0.78 and 0.76 for the trochanteric and femoral neck regions, respectively, in differentiating osteoporosis from normal cases (22). In the study by Lim et al., a success rate exceeding 93% (CA, specificity, and negative predictive values) was achieved in predicting femoral osteoporosis using radiomics data from abdominopelvic CTs and ML algorithms (24).

In the study by He et al., which included 109 cases, radiomics data from lumbar MRI T1 and T2-weighted images and ML algorithms were utilized. AUC values for models created with data from T1-weighted images, T2-weighted images, and both were 0.772, 0.772, and 0.810, respectively, for differentiating normal from osteopenia; 0.724, 0.682, and 0.797 for differentiating normal from osteoporosis; and 0.730, 0.734, and 0.769 for differentiating osteopenia from osteoporosis (14). While BMD values were categorized as osteoporosis, osteopenia, and normal in some of these studies, the

diagnostic performance of the Naive Bayes model in our study was higher for differentiating osteoporosis (Table 3).

Recent studies have also explored automated techniques. An automated method was described for detecting early-stage osteoporosis using cortical radiogram metric measures and trabecular texture analysis from hand and wrist radiographs (25). Zhao et al. developed a fully automated radiomics pipeline with deep learning-based segmentation using the DIXON sequence at six echo times with a short TE time in the lumbar region to demonstrate osteoporosis and abnormal bone density. They reported a model with success comparable to manual segmentation for BMD classification (26).

In the literature, some studies have used data obtained from CT, dental panoramic radiography, and radiographs to predict osteoporosis using deep learning algorithms, beyond classical ML approaches (27-31). Dai et al. demonstrated that BMD values from DEXA could be estimated by a model created with radiomics data from abdominal CT (32).

In the study by Burian et al., texture analysis was performed using classical statistical methods on chemical shift images to examine differences in bone marrow between pre- and postmenopausal women, with a focus on the proton density fat fraction (17). Additionally, various studies using deep learning and ML have investigated bone properties (29, 33).

There are also studies focused on detecting or predicting vertebral fractures. In a study by Ramos et al. involving 47 patients, the new ML model BEAUT (BonE Analysis Using Texture), developed using radiomics features from lumbar MRI T2-weighted images, was more effective at predicting fragility fractures than other ML models (CA 0.92, AUC 0.97) (34). In another study by Valentinitich et al., a model combining three-dimensional texture features with regional volumetric BMD of the entire thoracolumbar spine showed high discrimination performance in detecting vertebral fractures, outperforming the diagnostic success of volumetric BMD alone (35).

Similar to our findings, numerous publications have described the relationship between low BMD, BMI, and body weight (36-40). In our study, the height and age variables did not show a significant difference in the osteoporotic group ($P > 0.05$). In the study by

Ozeraitiene and Butenaite, it was noted that anthropometric measurements such as body weight, BMI, and skinfold thickness were lower in cases of osteoporosis (41). In the study by Mikula et al., prospective stature shortening was found to be an effective method for identifying patients with vertebral fractures, vitamin D deficiency, and low BMD. While the absence of stature shortening does not exclude these diagnoses, its presence supports a high positive likelihood ratio (42).

In the review by Yedavally-Yellayi et al., it is stated that significant stature shortening in men and women aged 50 and over is a risk factor warranting vertebral imaging (43). Advanced age is a well-known risk factor for low BMD (1, 2, 43). The high mean age of the patients in our study may explain the lack of a statistically significant age difference between the osteoporotic and non-osteoporotic groups (mean 65.32, standard deviation 8.50).

The statistically significant differences in body weight and BMI between the osteoporotic and non-osteoporotic groups are noteworthy. These factors could potentially influence the radiomics features extracted from MRI images, as body composition might affect tissue properties and, consequently, the radiomics signatures. Differences in body weight and BMI might also impact the performance of machine learning models by introducing bias related to these physical attributes. To mitigate these potential influences, future studies could consider using Z-scores for body weight and BMI, standardizing these variables relative to the population mean and standard deviation. This approach could help minimize the impact of body composition differences on radiomics feature extraction and model performance. Additionally, including body weight and BMI as covariates in the analysis could provide more robust results, ensuring that the observed differences are not solely attributable to these factors.

Selecting five features using the FCBF method effectively reduced the dimensionality of the dataset while retaining the most relevant predictive information. This decision was based on preliminary analyses, which suggested that this number provided a good balance between model complexity and performance. While this approach reduces the risk of overfitting, it is essential to validate these findings with larger datasets. Future studies should explore the impact of selecting different numbers of features on

model performance and generalizability to ensure optimal outcomes.

Apart from the retrospective nature of our study, there were some limitations. One significant limitation is the low number of male cases, with only 8 male participants out of a total of 140 cases. This gender imbalance reflects the higher prevalence of osteoporosis in women but poses a challenge for the generalizability of our findings. The predominance of female cases may limit the applicability of our results to the male population, which could exhibit different patterns and responses to osteoporosis. Future studies should aim to include a larger and more balanced sample size with more male participants to ensure that the findings are generalizable to both genders. This approach would enhance the robustness and applicability of the results across different demographics.

Instead of the hold-out cross-validation, the stratified 10-fold cross-validation technique was preferred, as the number of cases was limited, and the use of hold-out cross-validation would further reduce the dataset size. The lack of external validation with an independent dataset is another important limitation. Although the maximum one-year interval between the two examinations was set as an inclusion criterion and might seem relatively long, statistical analysis of the interval showed that DEXA and MRI examinations were frequently taken at close intervals (median difference of 1 month, with an interquartile range of 3.44 months).

In conclusion, we defined an ML model with good performance in the diagnosis of osteoporosis by using radiomics features obtained from lumbar MRI ADC maps. We also determined the threshold values at which each radiomics feature performed optimally. In the future, larger-scale prospective studies with a balanced male-to-female ratio and the use of ML and radiomics data from multiparametric MRI sequences could be transformative in diagnosing osteoporosis.

Footnotes

Authors' Contribution: F. E.: Conceptualization, methodology, software, formal analysis; writing-original draft; E. A.: Supervision, resources; G. D.: Supervision; B. Y. K.: Supervision, project administration; E. B.: Supervision.

Conflict of Interests Statement: The authors declared that they have no conflict of interest.

Data Availability: The dataset presented in the study is available on request from the corresponding author during submission or after publication. The data are not publicly available due to the general stance of the ministry of health.

Funding/Support: There was no specific grant from a funding agency in the public, commercial, or not-for-profit sectors for this research.

References

1. No authors listed. Consensus development conference: diagnosis, prophylaxis, and treatment of osteoporosis. *Am J Med.* 1993;**94**(6):646-50. [PubMed ID: [8506892](#)]. [https://doi.org/10.1016/0002-9343\(93\)90218-e](https://doi.org/10.1016/0002-9343(93)90218-e).
2. Nih Consensus Development Panel on Osteoporosis Prevention D; Therapy. Osteoporosis prevention, diagnosis, and therapy. *JAMA.* 2001;**285**(6):785-95. [PubMed ID: [11176917](#)]. <https://doi.org/10.1001/jama.285.6.785>.
3. Kanis JA. Assessment of fracture risk and its application to screening for postmenopausal osteoporosis: synopsis of a WHO report. WHO Study Group. *Osteoporos Int.* 1994;**4**(6):368-81. [PubMed ID: [7696835](#)]. <https://doi.org/10.1007/BF01622200>.
4. Kanis JA, Delmas P, Burckhardt P, Cooper C, Torgerson D. Guidelines for diagnosis and management of osteoporosis. The European Foundation for Osteoporosis and Bone Disease. *Osteoporos Int.* 1997;**7**(4):390-406. [PubMed ID: [9373575](#)]. <https://doi.org/10.1007/BF01623782>.
5. Abdulazeez RAJ, Tawfeeq RHA, Noori FA. Role of T1 Weighted and Diffusion Weighted Magnetic Resonance imaging application in the diagnosis of osteoporosis in lumbar spine in postmenopausal women. *Univ Thi-Qar J Med.* 2017;**14**(2):158-73.
6. Cvijetic S, Korsic M. Apparent bone mineral density estimated from DXA in healthy men and women. *Osteoporos Int.* 2004;**15**(4):295-300. [PubMed ID: [14628108](#)]. <https://doi.org/10.1007/s00198-003-1525-x>.
7. Guerri S, Mercatelli D, Aparisi Gomez MP, Napoli A, Battista G, Guglielmi G, et al. Quantitative imaging techniques for the assessment of osteoporosis and sarcopenia. *Quant Imaging Med Surg.* 2018;**8**(1):60-85. [PubMed ID: [29541624](#)]. [PubMed Central ID: [PMC5835658](#)]. <https://doi.org/10.21037/qims.2018.01.05>.
8. Oo WM, Naganathan V, Bo MT, Hunter DJ. Clinical utilities of quantitative ultrasound in osteoporosis associated with inflammatory rheumatic diseases. *Quant Imaging Med Surg.* 2018;**8**(1):100-13. [PubMed ID: [29541626](#)]. [PubMed Central ID: [PMC5835660](#)]. <https://doi.org/10.21037/qims.2018.02.02>.
9. Gazzotti S, Aparisi Gomez MP, Schileo E, Taddei F, Sangiorgi L, Fusaro M, et al. High-resolution peripheral quantitative computed tomography: research or clinical practice? *Br J Radiol.* 2023;**96**(1150):20221016. [PubMed ID: [37195008](#)]. [PubMed Central ID: [PMC10546468](#)]. <https://doi.org/10.1259/bjr.20221016>.
10. Meunier P, Aaron J, Edouard C, Vignon G. Osteoporosis and the replacement of cell populations of the marrow by adipose tissue. A

- quantitative study of 84 iliac bone biopsies. *Clin Orthop Relat Res*. 1971;**80**:147-54. [PubMed ID: 5133320]. <https://doi.org/10.1097/00003086-197110000-00021>.
11. Verma S, Rajaratnam JH, Denton J, Hoyland JA, Byers RJ. Adipocytic proportion of bone marrow is inversely related to bone formation in osteoporosis. *J Clin Pathol*. 2002;**55**(9):693-8. [PubMed ID: 12195001]. [PubMed Central ID: PMC1769760]. <https://doi.org/10.1136/jcp.55.9.693>.
 12. Fanucci E, Manenti G, Masala S, Laviani F, Di Costanzo G, Ludovici A, et al. Multiparameter characterisation of vertebral osteoporosis with 3-T MR. *Radiol Med*. 2007;**112**(2):208-23. [PubMed ID: 17361375]. <https://doi.org/10.1007/s11547-007-0136-6>.
 13. Griffith JF, Yeung DK, Antonio GE, Wong SY, Kwok TC, Woo J, et al. Vertebral marrow fat content and diffusion and perfusion indexes in women with varying bone density: MR evaluation. *Radiology*. 2006;**241**(3):831-8. [PubMed ID: 17053202]. <https://doi.org/10.1148/radiol.2413051858>.
 14. He L, Liu Z, Liu C, Gao Z, Ren Q, Lei L, et al. Radiomics Based on Lumbar Spine Magnetic Resonance Imaging to Detect Osteoporosis. *Acad Radiol*. 2021;**28**(6):e165-71. [PubMed ID: 32386949]. <https://doi.org/10.1016/j.acra.2020.03.046>.
 15. Yeung DK, Wong SY, Griffith JF, Lau EM. Bone marrow diffusion in osteoporosis: evaluation with quantitative MR diffusion imaging. *J Magn Reson Imaging*. 2004;**19**(2):222-8. [PubMed ID: 14745757]. <https://doi.org/10.1002/jmri.10453>.
 16. Hatipoglu HG, Selvi A, Ciliz D, Yuksel E. Quantitative and diffusion MR imaging as a new method to assess osteoporosis. *AJNR Am J Neuroradiol*. 2007;**28**(10):1934-7. [PubMed ID: 17905893]. [PubMed Central ID: PMC8134234]. <https://doi.org/10.3174/ajnr.A0704>.
 17. Burian E, Subburaj K, Mookiah MRK, Rohrmeier A, Hedderich DM, Dieckmeyer M, et al. Texture analysis of vertebral bone marrow using chemical shift encoding-based water-fat MRI: a feasibility study. *Osteoporos Int*. 2019;**30**(6):1265-74. [PubMed ID: 30903208]. [PubMed Central ID: PMC6546652]. <https://doi.org/10.1007/s00198-019-04924-9>.
 18. Li GW, Xu Z, Chen QW, Tian YN, Wang XY, Zhou L, et al. Quantitative evaluation of vertebral marrow adipose tissue in postmenopausal female using MRI chemical shift-based water-fat separation. *Clin Radiol*. 2014;**69**(3):254-62. [PubMed ID: 24286935]. <https://doi.org/10.1016/j.crad.2013.10.005>.
 19. Karampinos DC, Ruschke S, Dieckmeyer M, Diefenbach M, Franz D, Gersing AS, et al. Quantitative MRI and spectroscopy of bone marrow. *J Magn Reson Imaging*. 2018;**47**(2):332-53. [PubMed ID: 28570033]. [PubMed Central ID: PMC581907]. <https://doi.org/10.1002/jmri.25769>.
 20. Tang GY, Lv ZW, Tang RB, Liu Y, Peng YF, Li W, et al. Evaluation of MR spectroscopy and diffusion-weighted MRI in detecting bone marrow changes in postmenopausal women with osteoporosis. *Clin Radiol*. 2010;**65**(5):377-81. [PubMed ID: 20380936]. <https://doi.org/10.1016/j.crad.2009.12.011>.
 21. Taşkin G. The value of apparent diffusion coefficient measurements in the differential diagnosis of vertebral bone marrow lesions. *Turkish Journal of Medical Sciences*. 2013. <https://doi.org/10.3906/sag-1204-85>.
 22. Rastegar S, Vaziri M, Qasempour Y, Akhsh MR, Abdalvand N, Shiri I, et al. Radiomics for classification of bone mineral loss: A machine learning study. *Diagn Interv Imaging*. 2020;**101**(9):599-610. [PubMed ID: 32033913]. <https://doi.org/10.1016/j.diii.2020.01.008>.
 23. Mookiah MRK, Subburaj K, Mei K, Kopp FK, Kaesmacher J, Jungmann PM, et al. Multidetector Computed Tomography Imaging: Effect of Sparse Sampling and Iterative Reconstruction on Trabecular Bone Microstructure. *J Comput Assist Tomogr*. 2018;**42**(3):441-7. [PubMed ID: 29489591]. <https://doi.org/10.1097/RCT.0000000000000710>.
 24. Lim HK, Ha HI, Park SY, Han J. Prediction of femoral osteoporosis using machine-learning analysis with radiomics features and abdomen-pelvic CT: A retrospective single center preliminary study. *PLoS One*. 2021;**16**(3). e0247330. [PubMed ID: 33661911]. [PubMed Central ID: PMC7932154]. <https://doi.org/10.1371/journal.pone.0247330>.
 25. Areeckal AS, Jayasheelan N, Kamath J, Zawadynski S, Kocher M, David SS. Early diagnosis of osteoporosis using radiogrammetry and texture analysis from hand and wrist radiographs in Indian population. *Osteoporos Int*. 2018;**29**(3):665-73. [PubMed ID: 29198076]. <https://doi.org/10.1007/s00198-017-4328-1>.
 26. Zhao Y, Zhao T, Chen S, Zhang X, Serrano Sosa M, Liu J, et al. Fully automated radiomic screening pipeline for osteoporosis and abnormal bone density with a deep learning-based segmentation using a short lumbar mDixon sequence. *Quant Imaging Med Surg*. 2022;**12**(2):1198-213. [PubMed ID: 3511616]. [PubMed Central ID: PMC8739149]. <https://doi.org/10.21037/qims-21-587>.
 27. Lee KS, Jung SK, Ryu JJ, Shin SW, Choi J. Evaluation of Transfer Learning with Deep Convolutional Neural Networks for Screening Osteoporosis in Dental Panoramic Radiographs. *J Clin Med*. 2020;**9**(2). [PubMed ID: 32024114]. [PubMed Central ID: PMC7074309]. <https://doi.org/10.3390/jcm9020392>.
 28. Yamamoto N, Sukegawa S, Kitamura A, Goto R, Noda T, Nakano K, et al. Deep Learning for Osteoporosis Classification Using Hip Radiographs and Patient Clinical Covariates. *Biomolecules*. 2020;**10**(11). [PubMed ID: 33182778]. [PubMed Central ID: PMC7697189]. <https://doi.org/10.3390/biom10111534>.
 29. Smets J, Shevroja E, Hugle T, Leslie WD, Hans D. Machine Learning Solutions for Osteoporosis-A Review. *J Bone Miner Res*. 2021;**36**(5):833-51. [PubMed ID: 33751686]. <https://doi.org/10.1002/jbmr.4292>.
 30. Zhang B, Yu K, Ning Z, Wang K, Dong Y, Liu X, et al. Deep learning of lumbar spine X-ray for osteopenia and osteoporosis screening: A multicenter retrospective cohort study. *Bone*. 2020;**140**:115561. [PubMed ID: 32730939]. <https://doi.org/10.1016/j.bone.2020.115561>.
 31. Yasaka K, Akai H, Kunimatsu A, Kiryu S, Abe O. Prediction of bone mineral density from computed tomography: application of deep learning with a convolutional neural network. *Eur Radiol*. 2020;**30**(6):3549-57. [PubMed ID: 32060712]. <https://doi.org/10.1007/s00330-020-06677-0>.
 32. Dai H, Wang Y, Fu R, Ye S, He X, Luo S, et al. Radiomics and stacking regression model for measuring bone mineral density using abdominal computed tomography. *Acta Radiol*. 2023;**64**(1):228-36. [PubMed ID: 34964365]. <https://doi.org/10.1177/02841851211068149>.
 33. Pang S, Su Z, Leung S, Nachum IB, Chen B, Feng Q, et al. Direct automated quantitative measurement of spine by cascade amplifier regression network with manifold regularization. *Med Image Anal*. 2019;**55**:103-15. [PubMed ID: 31048199]. <https://doi.org/10.1016/j.media.2019.04.012>.
 34. Ramos JS, Maciel JG, Cazzolato MT, Traina C, Nogueira-Barbosa MH, Traina AJ. BEAUT: a radiomic approach to identify potential lumbar fractures in magnetic resonance imaging. *2021 IEEE 34th International Symposium on Computer-Based Medical Systems (CBMS)*. 2021. p. 389-94.
 35. Valentinitich A, Trebeschi S, Kaesmacher J, Lorenz C, Löffler MT, Zimmer C, et al. Opportunistic osteoporosis screening in multi-detector CT images via local classification of textures. *Osteoporos Int*.

- 2019;**30**(6):1275-85. [PubMed ID: 30830261]. [PubMed Central ID: PMC6546649]. <https://doi.org/10.1007/s00198-019-04910-1>.
36. Ravn P, Cizza G, Bjarnason NH, Thompson D, Daley M, Wasnich RD, et al. Low body mass index is an important risk factor for low bone mass and increased bone loss in early postmenopausal women. Early Postmenopausal Intervention Cohort (EPIC) study group. *J Bone Miner Res.* 1999;**14**(9):1622-7. [PubMed ID: 10469292]. <https://doi.org/10.1359/jbmr.1999.14.9.1622>.
37. Salamat MR, Salamat AH, Abedi I, Janghorbani M. Relationship between Weight, Body Mass Index, and Bone Mineral Density in Men Referred for Dual-Energy X-Ray Absorptiometry Scan in Isfahan, Iran. *J Osteoporos.* 2013;**2013**:205963. [PubMed ID: 24222888]. [PubMed Central ID: PMC3814102]. <https://doi.org/10.1155/2013/205963>.
38. Bjarnason NH, Christiansen C. The influence of thinness and smoking on bone loss and response to hormone replacement therapy in early postmenopausal women. *J Clin Endocrinol Metab.* 2000;**85**(2):590-6. [PubMed ID: 10690860]. <https://doi.org/10.1210/jcem.85.2.6364>.
39. Black DM, Steinbuch M, Palermo L, Dargent-Molina P, Lindsay R, Hoeslyni MS, et al. An assessment tool for predicting fracture risk in postmenopausal women. *Osteoporos Int.* 2001;**12**(7):519-28. [PubMed ID: 11527048]. <https://doi.org/10.1007/s001980170072>.
40. Felson DT, Zhang Y, Hannan MT, Anderson JJ. Effects of weight and body mass index on bone mineral density in men and women: the Framingham study. *J Bone Miner Res.* 1993;**8**(5):567-73. [PubMed ID: 8511983]. <https://doi.org/10.1002/jbmr.5650080507>.
41. Ozeraitiene V, Butenaite V. The evaluation of bone mineral density based on nutritional status, age, and anthropometric parameters in elderly women. *Medicina (Kaunas).* 2006;**42**(10):836-42. [PubMed ID: 17090984].
42. Mikula AL, Hetzel SJ, Binkley N, Anderson PA. Validity of height loss as a predictor for prevalent vertebral fractures, low bone mineral density, and vitamin D deficiency. *Osteoporos Int.* 2017;**28**(5):1659-65. [PubMed ID: 28154943]. <https://doi.org/10.1007/s00198-017-3937-z>.
43. Yedavally-Yellayi S, Ho AM, Patalinghug EM. Update on Osteoporosis. *Prim Care.* 2019;**46**(1):175-90. [PubMed ID: 30704657]. <https://doi.org/10.1016/j.pop.2018.10.014>.

Table 5. Threshold, Sensitivity, Specificity Values of the Radiomics Features Which had AUC Values Greater Than 0,70

Radiomics feature	AUC (%95 CI)	P	Threshold ^a	Sensitivity	Specificity
L1-4 log-sigma-3-0-mm-3D first order median ^b	0.742 (0.631 - 0.854)	0.0004	161.8236694	0.714	0.714
L1 wavelet-LHH first order range ^b	0.742 (0.627 - 0.856)	0.0004	772.300293	0.857	0.580
L2-4 log-sigma-3-0-mm-3D first order median ^b	0.74 (0.631 - 0.85)	0.0005	130.8338051	0.905	0.513
L1 wavelet-LHH GLDM high gray Level emphasis ^b	0.733 (0.633 - 0.833)	0.0007	12426.98297	0.762	0.655
L1 wavelet-LHL GLDM large dependence high gray level emphasis ^b	0.728 (0.623 - 0.834)	0.0009	316.7002581	0.905	0.538
L1 wavelet-LHL gray level size zone matrix (GLSZM) small area emphasis ^b	0.726 (0.627 - 0.825)	0.0010	669.0405296	0.857	0.597
L1 wavelet-LHL first order minimum ^b	0.726 (0.603 - 0.849)	0.0010	138.3913483	0.667	0.798
L4 log-sigma-3-0-mm-3D first order median ^b	0.723 (0.617 - 0.829)	0.0011	123.4394493	0.905	0.555
L1 wavelet-LHL neighborhood gray-tone difference Matrix (NGTDM) coarseness ^b	0.722 (0.623 - 0.821)	0.0012	820.7429058	0.952	0.487
L1 wavelet-LHL first order root mean squared ^b	0.721 (0.613 - 0.829)	0.0013	144355620.8	0.810	0.580
L1 wavelet-HHL GLSZM zone percentage ^b	0.72 (0.602 - 0.838)	0.0013	0.424339815	0.714	0.723
L1 wavelet-LHH NGTDM first order entropy ^b	0.72 (0.612 - 0.829)	0.0013	594726568.4	0.810	0.580
L1-4 log-sigma-3-0-mm-3D first order root mean squared ^b	0.719 (0.607 - 0.831)	0.0014	238.6731562	0.714	0.739
L1 wavelet-LHL first order variance ^b	0.719 (0.606 - 0.832)	0.0014	183.7174645	0.952	0.403
L1 wavelet-LHL gray level run length matrix (GLRLM) long run emphasis ^b	0.719 (0.607 - 0.831)	0.0014	56.88197474	0.952	0.403
L1 wavelet-HHL NGTDM complexity ^b	0.718 (0.6 - 0.836)	0.0015	0.676536483	0.714	0.723
L1 wavelet-LHL first order uniformity ^b	0.718 (0.593 - 0.843)	0.0015	5.645465978	0.571	0.857
L1 wavelet-LHL GLRLM gray level variance ^b	0.718 (0.605 - 0.831)	0.0015	33487.69379	0.952	0.403
L1 wavelet-LHL GLDM small dependence emphasis ^b	0.718 (0.605 - 0.831)	0.0015	53.66430712	0.952	0.403
L1-4 log-sigma-3-0-mm-3D first order mean ^b	0.718 (0.593 - 0.843)	0.0015	155.6497469	0.762	0.639
L1 wavelet-LHL GLRLM short run low gray level emphasis ^b	0.717 (0.608 - 0.826)	0.0015	2414.827911	0.905	0.471
L1 wavelet-LHL GLSZM size zone non-uniformity normalized ^b	0.717 (0.615 - 0.819)	0.0015	893.0282637	0.762	0.664
L1 wavelet-LHL GLRLM long run low gray level emphasis ^b	0.717 (0.615 - 0.819)	0.0015	849.1502259	0.762	0.664
L1 wavelet-LHL GLDM small dependence high gray level emphasis ^b	0.715 (0.614 - 0.817)	0.0017	883.5853389	0.762	0.664
L2 log-sigma-3-0-mm-3D first order median ^b	0.715 (0.59 - 0.841)	0.0017	182.5972176	0.619	0.824
L3 log-sigma-3-0-mm-3D first order root mean squared ^b	0.715 (0.609 - 0.821)	0.0017	221.0883332	0.810	0.622
L1 wavelet-HHL first order range ^b	0.715 (0.603 - 0.827)	0.0017	277.4433441	0.810	0.580
L1 wavelet-LHL gray level co-occurrence matrix (GLCM) Id ^b	0.714 (0.598 - 0.831)	0.0018	74.51247581	0.619	0.723
L1 wavelet-LHL GLSZM gray level non-uniformity normalized ^b	0.713 (0.597 - 0.83)	0.0018	5.074148459	0.619	0.782
L3 log-sigma-3-0-mm-3D first order median ^b	0.712 (0.601 - 0.823)	0.0020	154.2673759	0.714	0.672
L1-4 log-sigma-3-0-mm-3D first order 90percentile ^b	0.711 (0.596 - 0.826)	0.0021	374.7948471	0.714	0.748
L1 wavelet-LHL first order energy ^b	0.711 (0.592 - 0.83)	0.0021	239.8392797	0.524	0.815
L1 wavelet-LHL GLCM lmc2 ^b	0.711 (0.607 - 0.815)	0.0021	802.288168	0.762	0.639
L1 wavelet-LHL GLCM IDM ^b	0.71 (0.594 - 0.826)	0.0022	90.46296759	0.619	0.731
L2-4 log-sigma-3-0-mm-3D first order root mean squared ^b	0.709 (0.601 - 0.818)	0.0023	226.992795	0.714	0.681
L3 log-sigma-3-0-mm-3D NGTDM busyness ^a	0.709 (0.604 - 0.814)	0.0023	0.368800857	0.905	0.471
L2-4 log-sigma-3-0-mm-3D first order mean ^b	0.708 (0.586 - 0.83)	0.0024	145.8226851	0.762	0.588
L1 wavelet-LHL first order kurtosis ^a	0.707 (0.601 - 0.814)	0.0025	-640.053894	0.762	0.622
L1 wavelet-HHL GLCM Cluster prominence ^a	0.707 (0.604 - 0.81)	0.0025	0.093677529	0.857	0.529
L1 wavelet-LHL GLSZM Small Area high gray level emphasis ^a	0.707 (0.592 - 0.821)	0.0026	0.04102843	0.905	0.471
L1 wavelet-LHL first order mean ^b	0.706 (0.584 - 0.829)	0.0026	4.713948691	0.571	0.807
L1 wavelet-LHL GLCM IDMN ^b	0.706 (0.601 - 0.811)	0.0026	27.3785354	0.762	0.622
L1 wavelet-LHL GLCM joint energy ^b	0.706 (0.601 - 0.811)	0.0026	54.75707079	0.762	0.622
L1 wavelet-LHL GLRLM run length non-uniformity normalized ^b	0.706 (0.603 - 0.809)	0.0026	831.1979223	0.952	0.454
L1 wavelet-LHL GLCM sum entropy ^b	0.705 (0.59 - 0.821)	0.0028	47.99747138	0.714	0.605
L1 wavelet-HHL GLCM joint average ^a	0.705 (0.585 - 0.824)	0.0028	0.140912352	0.762	0.639
L3 wavelet-LH first order median ^b	0.704 (0.565 - 0.843)	0.0029	70.33731461	0.571	0.815
L1 wavelet-LHL GLCM cluster tendency ^b	0.704 (0.591 - 0.817)	0.0029	575635.1876	0.810	0.571
L1 wavelet-LHL first order range ^b	0.703 (0.587 - 0.82)	0.0030	2222.682983	0.571	0.773
L2 wavelet-LLL GLCM difference average ^b	0.703 (0.613 - 0.793)	0.0031	18.4495188	1.000	0.479
L2 log-sigma-3-0-mm-3D GLSZM zone variance ^a	0.703 (0.597 - 0.809)	0.0031	45.36158539	0.714	0.647
L1 wavelet-LHL GLCM correlation ^b	0.702 (0.579 - 0.825)	0.0032	3.771944675	0.667	0.723
L2 log-sigma-3-0-mm-3D GLSZM large area emphasis ^a	0.702 (0.596 - 0.807)	0.0032	101.9358356	1.000	0.370
L1-4 wavelet-LLL GLCM difference variance ^b	0.702 (0.599 - 0.805)	0.0032	259.307057	0.857	0.529
L3 log-sigma-3-0-mm-3D first order 90percentile ^b	0.702 (0.594 - 0.809)	0.0032	362.6814285	0.714	0.731
L2 wavelet-LLL GLCM contrast ^b	0.701 (0.611 - 0.792)	0.0033	619.6491217	0.952	0.521
L1 wavelet-LLL GLDM high gray level emphasis ^b	0.701 (0.591 - 0.81)	0.0034	269.6090191	0.857	0.504
L2-4 log-sigma-3-0-mm-3D first order 90 percentile ^b	0.7 (0.589 - 0.811)	0.0035	357.1382874	0.762	0.681

^a Threshold values are defined by Youden Index.

^b Larger test result indicates more positive test.

^c Smaller test result indicates more positive test.
